ACS APPLIED MATERIALS & INTERFACES

www.acsami.org

Research Article

Soft-Shear-Aligned Vertically Oriented Lamellar Block Copolymers for Template-Free Sub-10 nm Patterning and Hybrid Nanostructures

Maninderjeet Singh, Aman Agrawal, Wenjie Wu, Ali Masud, Edward Armijo, Damian Gonzalez, Shenghui Zhou, Tanguy Terlier, Chenhui Zhu, Joseph Strzalka, Krzysztof Matyjaszewski, Michael Bockstaller, Jack F. Douglas, and Alamgir Karim*

Cite This: *ACS Appl. Mater. Interfaces* 2022, 14, 12824–12835

Read Online

ACCESS | Metrics & More | Article Recommendations | Supporting Information

ABSTRACT: The template-free unidirectional alignment of lamellar block copolymers (*l*-BCPs) for sub-10 nm high-resolution patterning and hybrid multicomponent nanostructures is important for technological applications. We demonstrate a modified soft-shear-directed self-assembly (SDSA) approach for aligning pristine *l*-BCPs and *l*-BCPs with incorporated polymer-grafted nanoparticles (PGNPs), as well as the *l*-BCP conversion to aligned gold nanowires, and hybrid of metallic gold nanowire and dielectric silica nanoparticle in the form of line-dot nanostructures. The smallest patterns have a half-pitch as small as 9.8 nm. In all cases, soft-shear is achieved using a high-molecular-mass polymer topcoat layer, with support on a neutral bottom layer. We also show that the hybrid line-dot nanostructures have a red-shifted plasmonic response in comparison to neat gold nanowires. These template-free aligned BCPs and nanowires have potential use in nanopatterning applications, and the line-dot nanostructures should be useful in the sensing of biomolecules and other molecular species based on the plasmonic response of the nanowires.

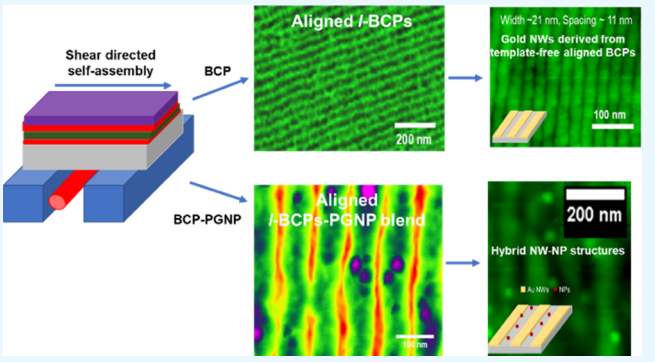

KEYWORDS: *block copolymers, template-free alignment, sub-10 nm patterning, self-assembly, aligned nanowires, polymer-grafted nanoparticles, hybrid nanowire−nanoparticle structures, plasmonic resonance*

INTRODUCTION

Block copolymer (BCP) self-assembly in thin films holds immense potential for generating sub-10 nm nanostructures[1] to fulfill the growing demand for miniaturization of electronic devices[2] and smart nanomaterials[3,4] and for creating hybrid nanostructures having diverse multifunctional properties desired in next-generation optical and electronic circuitry.[5] Directed self-assembly (DSA) of BCPs has emerged as a powerful tool for density multiplication of photolithographically defined features using lamellar,[1,6,7] cylindrical,[8,9] and spherical[10,11] BCPs. Vertically oriented[12,13] and aligned lamellar BCPs are most promising for creating line patterns for lithography due to their ability to generate symmetric sub-10 nm features and smooth wall profiles.[1] Current state-of-the-art methods combine photolithographic patterns for lamellar BCP alignment; however, aligning the lamellar BCPs without the photolithographic templates opens avenues for the use of BCPs in applications including nanopatterning on flexible substrates[14] for flexible electronics,[15] optical materials,[16,17] memory devices,[18] and energy storage materials.[19] Hybrid nanostructures, wherein different nanopatterns such as line-dot, line-line, or dot-dot of metal or dielectric materials can be combined to create unique functionalities for advanced applications; however, these are difficult to fabricate while controlling the precise nanostructure placement.[5]

Much of the progress in BCP lithography has been made using polystyrene-*block*-poly(methyl methacrylate) (PS-*b*-PMMA) owing to the small difference in the surface tension of PS and PMMA[1,20] for vertical order and lithographic etch properties of PMMA. Unfortunately, due to the lower Flory−Huggins interaction parameter (χ) between PS and PMMA, the resolution limit for PS-*b*-PMMA is limited to 12 nm.[21] Furthermore, the BCP systems having higher χ have significantly different surface tension between the polymer blocks, which demands the need for neutral substrate surface and topcoats[1,22] for controlling the BCP orientation. Using neutral topcoats, high χ BCPs have been aligned using DSA on chemically patterned substrates to form sub-10 nm channels.[1,23]

Received: December 9, 2021
Accepted: February 21, 2022
Published: March 4, 2022

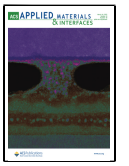

https://doi.org/10.1021/acsami.1c23865
ACS Appl. Mater. Interfaces 2022, 14, 12824−12835

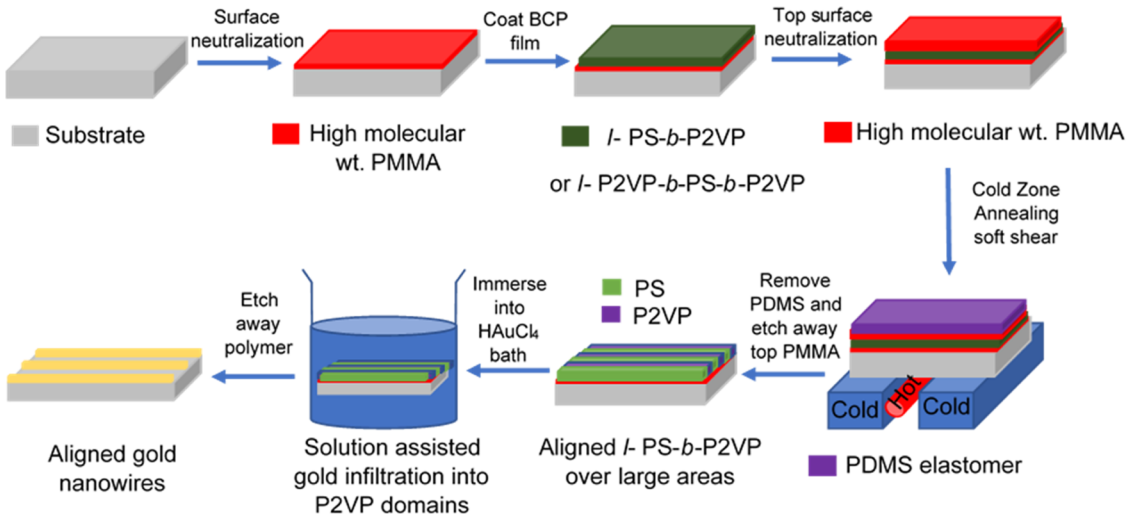

Figure 1. Schematic showing the process used for the template-free alignment of lamellar polystyrene-*block*-poly(2-vinyl pyridine) (diblock *l*-PS-*b*-P2VP and triblock *l*-P2VP-*b*-PS-*b*-P2VP) and subsequent gold nanowires.

On the other hand, hybrid nanostructures or multiple nanocomponents have been achieved using colloidal assembly, which is usually complex in nature.[24−26] The complex colloidal assembly is usually accomplished using electrostatic[26,27] or biomolecular interactions.[25] However, scaling up such nanostructures or making precise line-dot structures using these methods is very challenging. BCP self-assembly has also been employed to make hybrid nanostructures by two-layer BCP patterning[5,28] .Here, the first BCP layer was used to develop metallic line or dot pattern using metal ion infiltration and the second BCP layer was deposited and metal ion infiltrated on top to make hybrid metal nanostructures or nano transfer printing followed by BCP assembly,[29] wherein the first layer is developed using nano transfer printing and the second layer is made using ion infiltration into self-assembled BCP layers. This bilayered BCP assembly suffers from the challenges of uncontrolled second layer placement for applications, wherein precise control over nanostructures is desired and is limited to nanostructures that can be derived by ion infiltration of BCP structures. The aligned BCP/polymer-grafted nanoparticles (PGNP) blends have the potential of generating hybrid nanostructures by converting one of the blocks to metallic nanostructure by ion infiltration and using the PGNP core to generate a dot pattern. However, aligning BCP/PGNP nanostructures is difficult using photolithographic templates, given that the PGNP addition alters the commensurability condition for blend alignment, thereby requiring the need for designing different photolithographic template pitches for different PGNP loadings.

Shear alignment of BCPs in thin films has proven to be an efficient alternative approach to substrate pattern-directed DSA for the alignment of BCPs. Although parallel-oriented cylindrical BCPs have been aligned with good orientation control using shear-based assembly,[30−32] the shear-induced assembly of lamellar BCPs, which hold much higher technological significance due to their ability to generate symmetric line-space patterns and vertically etchable channels desired in the semiconductor industry,[1,5,36,37] has not been successful for generating template-free sub-10 nm half-pitch vertical nanostructures.[33,34] Recently, there have been efforts to achieve shear assembly of lamellar BCPs by transmitting shear through polymeric nanomosaic coatings[34] and filtered plasma coatings;[35] however, these processes require complex fabrication of neutral layers and have been demonstrated for half pitches of ≈25 nm and ≈10.75 nm on template-free surfaces, respectively. To push the limits of shear-aligned BCP half-pitch patterns below 10 nm, and to achieve the template-free, unidirectional alignment of lamellar BCP nanodomains needed for nanolithography, effective shear transmitting neutral homopolymers, which can be readily and easily used as topcoats, are needed. Additionally, shear-aligned BCP/PGNP blends can generate hybrid nanostructures on a variety of substrates without the need for commensurability conditions and are not limited to nanostructures developed by ion-infiltration processes, i.e., the nanostructures can be extended to multiple nanoparticles or even 1D nanorods,[36,37] which can be used as core materials for PGNPs due to the advances in polymer chemistry. Select partitioning of the PGNPs to the BCP domain can be exploited for creating different nanopatterning modalities.

In this work, we show the shear-directed self-assembly (SDSA) of high χ lamellar BCP polystyrene-*block*-poly(2-vinyl pyridine) (PS-*b*-P2VP) using a poly(methyl methacrylate) (PMMA) homopolymer as a neutral topcoat[38] and bottom layer as well. A novel feature is that high shear stress generated by our cold zone annealing-soft shear (CZA-SS)[15] method is transmitted to the BCP layer for template-free shear alignment of vertical BCP lamellae. Furthermore, this roll-to-roll (R2R) compatible SDSA technique generates vertically aligned lamellar BCPs over large areas having high orientation control between ±2.5° from the R2R motion direction. We extend the use of this SDSA method to order and align poly(2-vinyl pyridine)-*block*-polystyrene-*block*-poly(2-vinyl pyridine) (P2VP-*b*-PS-*b*-P2VP) triblock copolymer to generate sub-10 nm BCP channels (half-pitch = 9.8 nm). We incorporate gold into aligned *l*-BCPs using a modified solution-phase infiltration method[39] to form gold nanochannels, having channel widths of 21 and 12 nm, and channel spacings of 10 and 7 nm for diblock and triblock copolymers, respectively. These SDSA assembled and fully aligned BCPs with tunable pitch size, and metallic nanowires having dimensions smaller than or comparable to those fabricated by the state-of-the-art photolithography or EUV lithography,[40,41] can have direct applications in nanolithography and associated electronic devices.[42,43] Furthermore, we extend the use of shear-aligned BCPs to BCP/PGNP blends using high-molecular mass PS-*b*-P2VP BCP and PS-*g*-SiO_2 PGNP blends

https://doi.org/10.1021/acsami.1c23865
ACS Appl. Mater. Interfaces 2022, 14, 12824−12835

confined between the neutral PMMA topcoat and bottom layer. We use these aligned BCP/PGNP blends to generate hybrid metallic gold nanowire−dielectric SiO_2 nanoparticle structures by solution-phase ion infiltration and organic content etching. We show that hybrid nanostructures have a red-shifted plasmonic response, as compared to neat gold nanowires, which is attributed to the increase of the medium dielectric constant due to the presence of dielectric nanoparticles. These hybrid nanostructures with tunable plasmonic responses might serve as a platform for next-generation bio/chemical sensing applications.

RESULTS AND DISCUSSION

Shear-Directed Self-Assembly. We utilize shear-directed self-assembly to align PS-*b*-P2VP and P2VP-*b*-PS-*b*-P2VP BCPs confined between a relatively neutral high-molecular-mass PMMA polymer.[38] Figure 1 shows the schematics of the steps used for template-free alignment of BCPs and subsequent metal infiltration to generate aligned nanowires. Quartz substrates are used in this study owing to their lower thermal conductivity than silicon, which aids in generating a sharp temperature gradient over the CZA setup, resulting in high-magnitude shear stress generated by an overlayer elastomer expansion and contraction on top of the topcoat.[15] Thus, the single oscillatory BCP aligning shear stress by CZA-SS is transmitted to the BCP cast-film through the topcoat layer. It has been recently demonstrated that a sharp gradient can be generated over silicon substrates as well during laser zone annealing,[44] paving the way for the extension of our approach on silicon substrates. The high-molecular mass (600 kg/mol) PMMA having a thickness ≈18 nm is flow coated (or spun cast) on the substrate and is annealed at 220 °C for 30 min under vacuum to ensure the strong adsorption of polymer chains to the substrate by mainly polar interactions, tested by rinsing the PMMA film in moderately good solvent toluene. No observable film thickness reduction occurred in the annealed PMMA films (tested by an interferometer and film color), which indicates that the PMMA was strongly adsorbed onto the quartz substrate. The adsorbed PMMA bottom layer stability on solvent rinsing is shown in the Supporting Information, Figure S8. This strategy for surface neutralization for vertical orientation of PS-*b*-P2VP (25-*b*-25 kg/mol) and P2VP-*b*-PS-*b*-P2VP (9.5-*b*-17.5-*b*-9.5 kg/mol) is much easier and robust than the usually employed surface neutralization technique for controlling the BCP orientation, wherein small-molecular mass polymers having H-bonding end groups are physico-chemically tethered to the substrate surface.[45] Our BCP film is coated over the PMMA neutral layer on the quartz substrate, and a 24 nm thick topcoat of the same 600 kg/mol PMMA is floated on top of the BCP film to generate neutral interfaces on both sides of the BCP film. The use of PMMA as a photoresist in lithography makes it convenient to use PMMA as a surface neutralizing polymer layer for BCP lithography if the need arises for etching it. A conformal elastomeric poly(dimethylsiloxane) (PDMS) pad is placed over the trilayered polymer film for enabling an oscillatory soft shear, driven by the thermal expansion coefficient mismatch of PDMS (5× higher) relative to the underlying BCP film, as the assembly passes over the cold−hot−cold zones with temperature gradients of ∼50 °C/mm created by the CZA setup[15] (Supporting Information, Figure S2). In this setup, the shear stress is efficiently transmitted through the high-molecular mass (600 kg/mol) topcoat via viscoelastic coupling to the BCP layer, resulting in fully aligned BCP nanodomains.

Notably, low-molecular mass PMMA topcoat (4 kg/mol) intermixes with the BCP, and we do not observe any perpendicular orientation and alignment (Supporting Information, Figure S3). After the CZA-SS process is complete, the PDMS pad is removed, and the topcoat PMMA layer is etched using a controlled UV-Ozone etching system (generating 254 and 185 nm wavelengths) with etching rates of ≈2 nm/s for surface characterization. After etching the top PMMA layer, gold metal is infused into the P2VP chains by submerging the aligned BCPs into the aq. chloroauric acid ($HAuCl_4$) solution by modifying a process developed by Buriak and co-workers.[39] Subsequently, the polymer was etched off to reveal the aligned gold nanochannels.

Figure 2 shows the time-of-flight secondary ion mass spectrometry (ToF-SIMS) depth profiling of *l*-BCP films

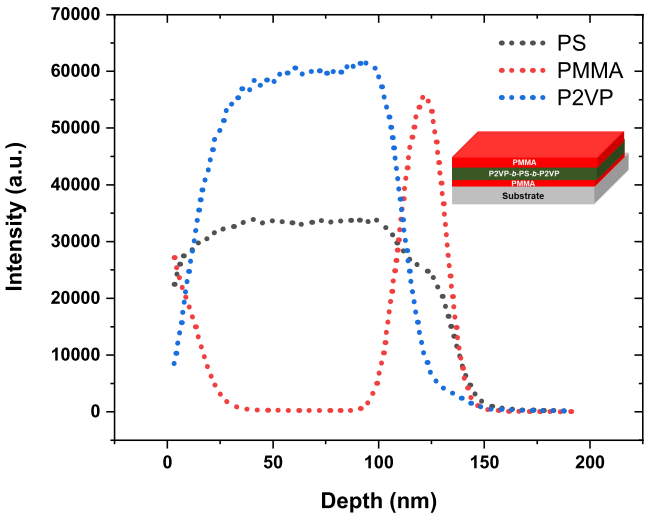

Figure 2. Time-of-flight secondary ion mass spectrometry (ToF-SIMS) depth profile of the *l*-BCP (P2VP-*b*-PS-*b*-P2VP) sandwiched between two neutral PMMA layers. ToF-SIMS depth profile shows the PMMA layer at the top and bottom of the *l*-BCP. The following polymers, PS, PMMA, and P2VP, have been characterized and monitored through the film, respectively, using C_2H^-, $C_4H_5O_2^-$, and CN^- ions. An argon cluster ion beam (Ar_{1500}^+, 10 keV with a typical current of 0.05 nA) has been used to etch the polymer structure.

sandwiched between the neutral top layer and bottom layer. ToF-SIMS is a highly sensitive technique for elemental and molecular characterization over 3D compositions and has been recently employed for morphology characterization of polymer-grafted nanoparticle films[37] and block copolymer morphologies.[46,47] The polystyrene (PS) polymer is characterized by the detection of C_2H^- ions, poly(methyl methacrylate) (PMMA) polymer is characterized by the detection of $C_4H_5O_2^-$, and poly(2-vinyl pyridine) (P2VP) polymer is characterized by the detections of CN^- ions. The ToF-SIMS depth profile shows the presence of the *l*-BCP film sandwiched between the neutral top layer and bottom layer. Furthermore, the ToF-SIMS demonstrates that the bottom PMMA layer is tethered to the substrate and does not intermix with the *l*-BCP film during film casting. The observed slope of the ion intensity vs depth profile at the polymer interfaces seems to be a result of induced roughening during the etching process, given that the ToF-SIMS is an invasive technique for characterization. It should be pointed out here that the PS and P2VP polymers do not follow the exact same trajectory, which might be due to the different etching rates

https://doi.org/10.1021/acsami.1c23865
ACS Appl. Mater. Interfaces 2022, 14, 12824−12835

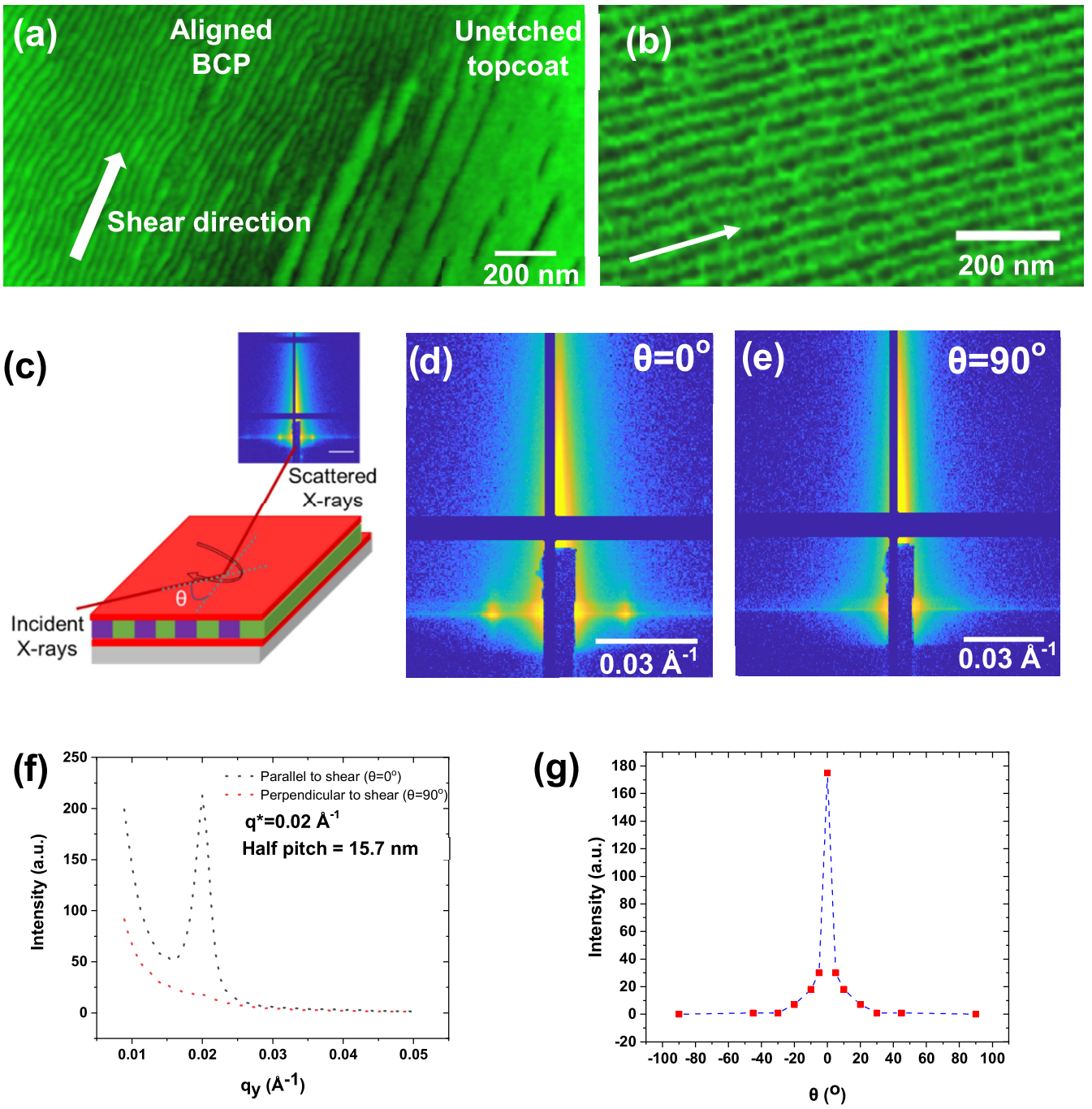

Figure 3. Shear-directed self-assembly induced alignment of the diblock polystyrene-*block*-poly(2-vinyl pyridine) (PS-*b*-P2VP) (25-*b*-25 kg/mol). (a) AFM height image of the shear-aligned BCPs underneath the homopolymer topcoat along with the unetched topcoat. (b) AFM phase image of the BCP after complete removal of topcoat. The arrows indicate the shear direction in (a, b). (c) Schematic for determining the large area alignment of the BCPs using GISAXS. (d) GISAXS image of the BCP film illuminated along the shear direction and (e) perpendicular to the shear direction. (f) 1D linecuts of the images in (d, e). (g) Intensity vs GISAXS scan angle (to the shear direction), showing all aligned BCPs over large areas.

of PS and P2VP by Bi_3+ ions. Furthermore, the surface roughening during the etching might make these anisotropic etching effects more predominant.

Figure 3 shows AFM images of the aligned PS-*b*-P2VP BCP film surface after the SDSA process demonstrating clear alignment along the soft-shear direction (Figure 3a). The topcoat and the BCP morphology are visible in the same image due to the anisotropic etching at the local scale. Furthermore, the AFM of the topcoat also shows aligned templating along the shear direction, indicative of the strong nature of CZA-SS shear forces. The macroscopic alignment of the BCP in the film interior was probed by grazing incidence-small angle X-ray scattering (GISAXS) above the BCP critical angle of 0.12°, and Figure 3c shows a schematic of probing the internal alignment in the film. The vertical streaks in Figure 3d of X-ray scattering patterns confirm the internal BCP film domain alignment in the film with vertical orientation along the soft-shear direction, obtained by probing along the shear direction at a random sample location of 1 in. × 1 in. areal dimensions on the wafer. Notably, perpendicular to the shear direction, no scattering is

https://doi.org/10.1021/acsami.1c23865
ACS Appl. Mater. Interfaces 2022, 14, 12824−12835

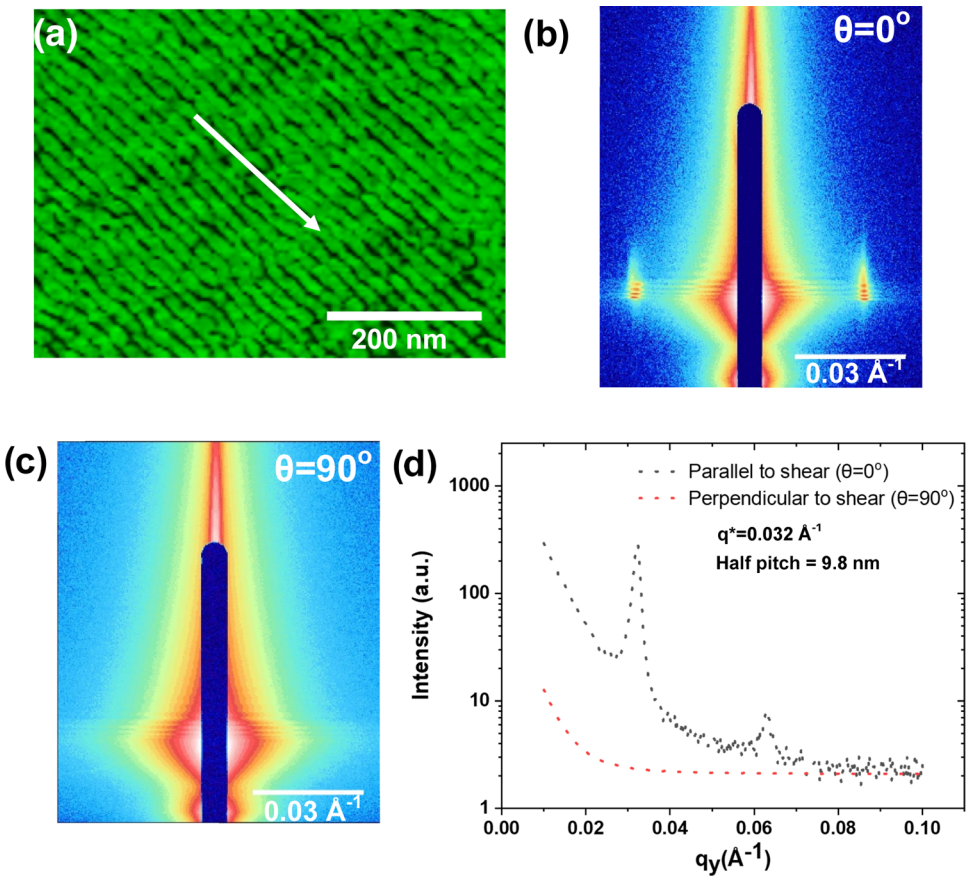

Figure 4. Soft-shear alignment of the triblock *l*-P2VP-*b*-PS-*b*-P2VP BCP for sub-10 nm patterning. (a) AFM phase image of the aligned BCPs after removal of the topcoat. The arrow indicates the shear direction. (b) GISAXS image of large area aligned BCPs along the shear direction and (c) perpendicular to the shear direction. (d) 1D linecuts of the GISAXS images in (b, c) showing alignment along the shear direction only. The domain size calculated from the peak position is 19.6 nm and the channel width is 9.8 nm.

observed, confirming a high degree of BCP alignment only along the shear direction (Figure 3e) across the entire 1 in.^{2} on the wafer. The high degree of BCP alignment is also confirmed with 1D linecuts along the Yoneda bands of the GISAXS images, as shown in Figure 3f. The diffraction intensity rapidly decreases even at angles as small as 5°, similar to the BCPs aligned using DSA,[48] with the alignment peak angular full width at half-maximum of alignment, FWHM ≈5° (Lorentz fit), again confirming that the BCP alignment is highly confined along the shear direction only, as demonstrated in Figure 3g. It should be noted that since the GISAXS measurements are performed on BCP films confined between two neutral layers, the diffraction peak intensity (along the shear) decreases as compared to the GISAXS intensity measured on films without any topcoat, which causes some broadening of the intensity vs angle curve. The domain sizes are extracted from the first peak position of the GISAXS linecuts across the scattered intensity. Mathematically, the domain size $(L_0) = 2\pi/q_0$, where q_0 is the first peak position in the GISAXS intensity vs inverse length scale. The pitch (domain size) calculated from GISAXS diffraction patterns is 31.4 nm, which translates to a half-pitch of 15.7 nm for diblock PS-*b*-P2VP.

SDSA for Sub-10 nm Patterning. For sub-10 nm patterning using BCPs, a low-molecular-mass P2VP-*b*-PS-*b*-P2VP triblock copolymer with a composition dictating a lamellar morphology is used in this study. Given the neutrality of the PMMA top and bottom layers with the PS and P2VP block, P2VP-*b*-PS-*b*-P2VP attains vertical orientation as well. Figure 4a shows the AFM image of the aligned P2VP-*b*-PS-*b*-P2VP BCPs after SDSA and topcoat removal, showing BCPs aligned along the shear direction. The film internal alignment of the BCP at a macroscopic level is confirmed by GISAXS in Figure 4b, which shows the vertical intensity streaks in the Q_y direction, orthogonal to the X-ray beam along the shear direction. As with the diblock BCP, when the X-ray beam is perpendicular to the shear direction on an arbitrary location on the substrate, no scattering is observed (Figure 4c), showing that the alignment is limited to the shear direction only. 1D linecuts of intensity in Q_y across the GISAXS images shown in Figure 4d show the high-intensity peak along the shear direction and no peak is perpendicular to the shear direction. The peak position shows the BCP pitch of around 19.6 nm, which translates to a half-pitch (channel width) of ≈9.8 nm.

Fabricating Gold Nanowires from SDSA-Aligned BCPs. We infiltrated gold into P2VP channels to make aligned gold nanochannels using the BCP templates by modifying a strategy pioneered by Buriak and co-workers.[39] In their study,[39] Chan et al. infiltrated metals into topographically aligned cylindrical BCPs using aqueous solutions. Furthermore, they used H^+ ions to swell the P2VP chains out of the PS matrix so that the metal ions could be intercalated into the P2VP chains.

Since the P2VP chains are directly exposed to the metal salt in the aqueous solution due to their lamellar morphology after topcoat etching, we did not require the addition of H^+ ions in the aq. solutions. Figure 5a shows a schematic of the intercalation of gold into P2VP chains when the aligned BCP film is submerged

https://doi.org/10.1021/acsami.1c23865
ACS Appl. Mater. Interfaces 2022, 14, 12824−12835

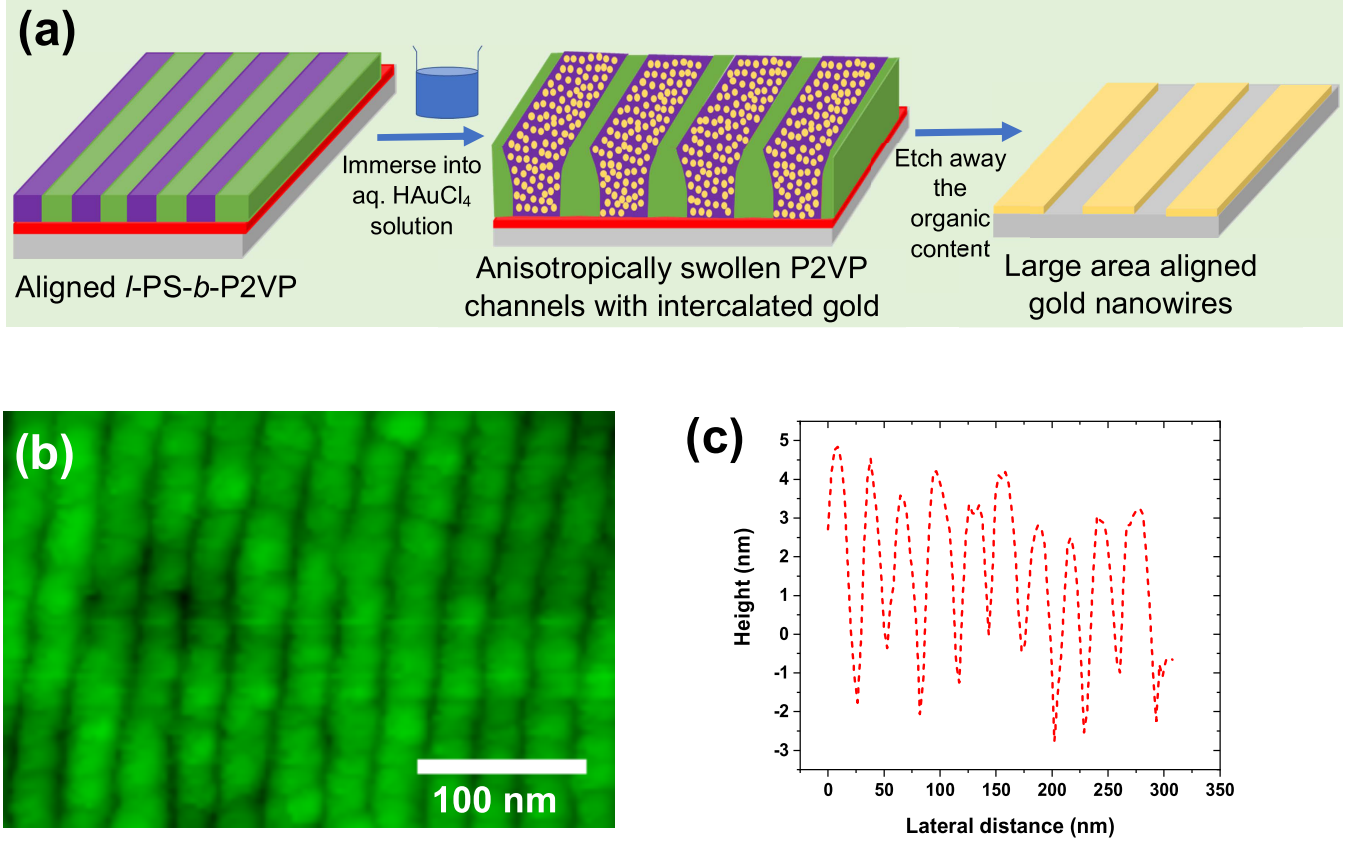

Figure 5. Fabrication of gold nanowires using aligned block copolymer templates. (a) Schematic illustrating the intercalation of gold into poly(2-vinyl pyridine) (P2VP) channels resulting in asymmetrically swollen P2VP channels, which are converted to gold nanochannels upon etching by ozone. (b) AFM height image of gold nanowires post etching of PS-*b*-P2VP (25-*b*-25) template. (c) Height profile of gold nanochannels from image (b) showing ≈6 nm high gold channels.

in the aqueous chloroauric acid ($HAuCl_4$) solution. The metal ions however do not interact with the PS chains as shown by Chan et al. The infiltration of gold into P2VP channels in the solution phase asymmetrically swells the P2VP diblock chains as shown in the schematic in Figure 5a, making the P2VP domains bigger than the PS domains. This swelling of P2VP is consistent with the observations of Chai et al.[39] and Lee et al.[49] The organic content inside the aligned BCPs is etched post gold infiltration, using ozone etching, leaving behind macroscopically aligned asymmetric gold nanochannels. Figure 5b shows an AFM image of ≈30 nm thick film of the diblock PS-*b*-P2VP BCP, with aligned gold nanochannels, post gold infiltration for 24 h followed by ozone etching of organics. The height of gold nanochannels is ≈6 nm, width is ≈21 nm, and the gap between the nanochannels is ≈10 nm, as shown in the height profile in Figure 5c. Likewise, an aligned ≈30 nm thick film of P2VP-*b*-PS-*b*-P2VP triblock copolymer film, submerged in the gold salt solution for 15 min, shows asymmetric gold channels with height ≈1.5 nm, width ≈12 nm, and gap ≈7 nm (refer to the SI, Figure S4). The successful fabrication of gold nanochannels has been confirmed by energy-dispersive X-ray analysis as well as shown in the Supporting Information, Figure S6. We note that gold nanochannels merge for immersion times greater than 15 min for triblock BCPs, due to the high degree of swelling of P2VP chains.

Alignment of Polymer-Grafted Nanoparticle-Block Copolymer Blends Using SDSA. The control of the alignment of inorganic nanoparticles at the nanoscale is of high technical importance, given that precisely aligned nanoparticles[50] can be used in applications ranging from data storage, electronics, chemical, and biological sensing and energy harvesting, etc. Aligned block copolymer/polymer-grafted nanoparticle (PGNP) blends provide a unique platform for precisely aligning inorganic particles in the desired fashion. The need for using PGNPs for precise particle alignment stems from the aggregation of bare nanoparticles in polymeric matrices. The BCP-PGNP blend alignment using traditional chemoepitaxial or graphoepitaxial methods is challenging given that the addition of nanoparticles changes the domain spacing of BCP-PGNP blends, thus altering the commensurability condition for the blend alignment. Furthermore, the epitaxial alignment is limited to substrates that can be patterned using photolithography. As such, the shear alignment of BCP/PGNP blend films possesses the potential of blend alignment on a variety of substrates. There have been efforts on the shear alignment of cylindrical BCPs and PGNP blends to align PGNP-containing BCPs;[5151] however, the alignment of cylindrical BCP-PGNP blends was observed to be distorted at PGNP loading higher than 1%, owing to the ligand dissociation at high temperature and polymer viscosity.

We demonstrate the shear alignment of PGNPs in the *l*-BCP matrix using shear-directed self-assembly of *l*-BCP-PGNP blend films confined between neutral PMMA layers. We use high-molecular-mass *l*-BCP (PS-*b*-P2VP with molecular mass 133,000-*b*-132,000 g/mol) for the localization and alignment of PGNPs. The PGNPs used in this study are synthesized using atom transfer radical polymerization (ATRP), and the synthesis details are mentioned elsewhere.[52] Briefly, PS-*g*-SiO_2 PGNPs have ≈16 nm (diameter) SiO_2 cores, an average of 360

https://doi.org/10.1021/acsami.1c23865
ACS Appl. Mater. Interfaces 2022, 14, 12824−12835

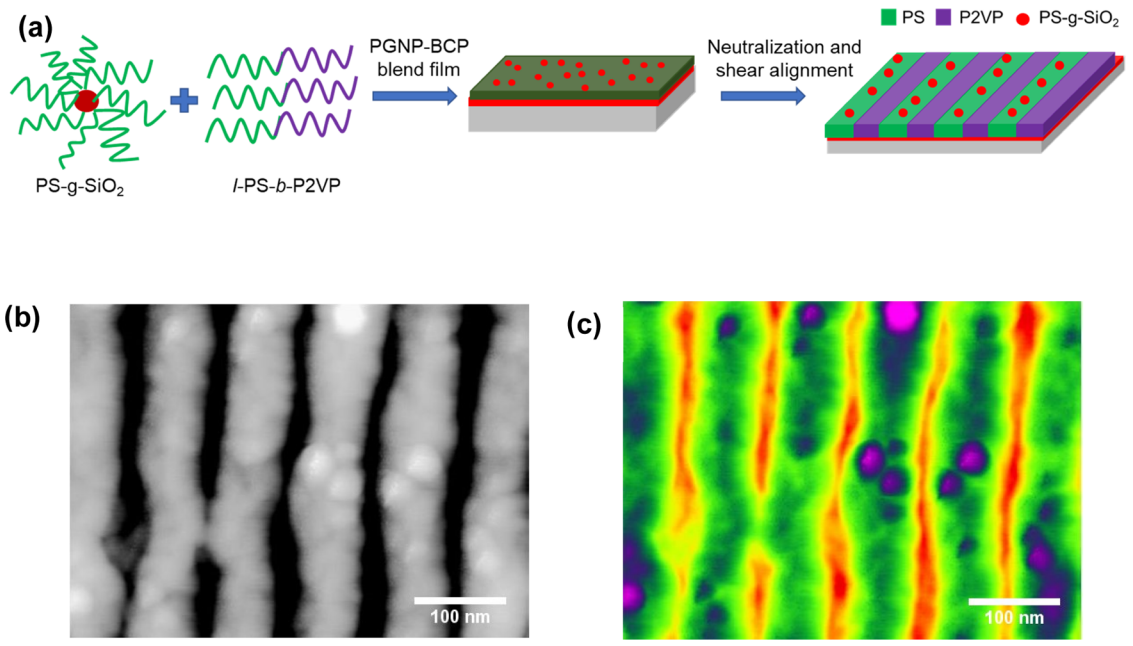

Figure 6. Shear alignment of high-molecular mass *l*-BCP (PS-*b*-P2VP) and PGNP (PS-*g*-SiO_2) blend systems for nanoparticle localization in aligned domains. (a) Schematics of the film preparation and alignment. (b) AFM height image showing aligned BCP-PGNP blends along the shear direction. (c) Color-coded AFM height image revealing the individual PGNPs (violet) confined to the PS channels (green) and no PGNPs present in the P2VP channels (red).

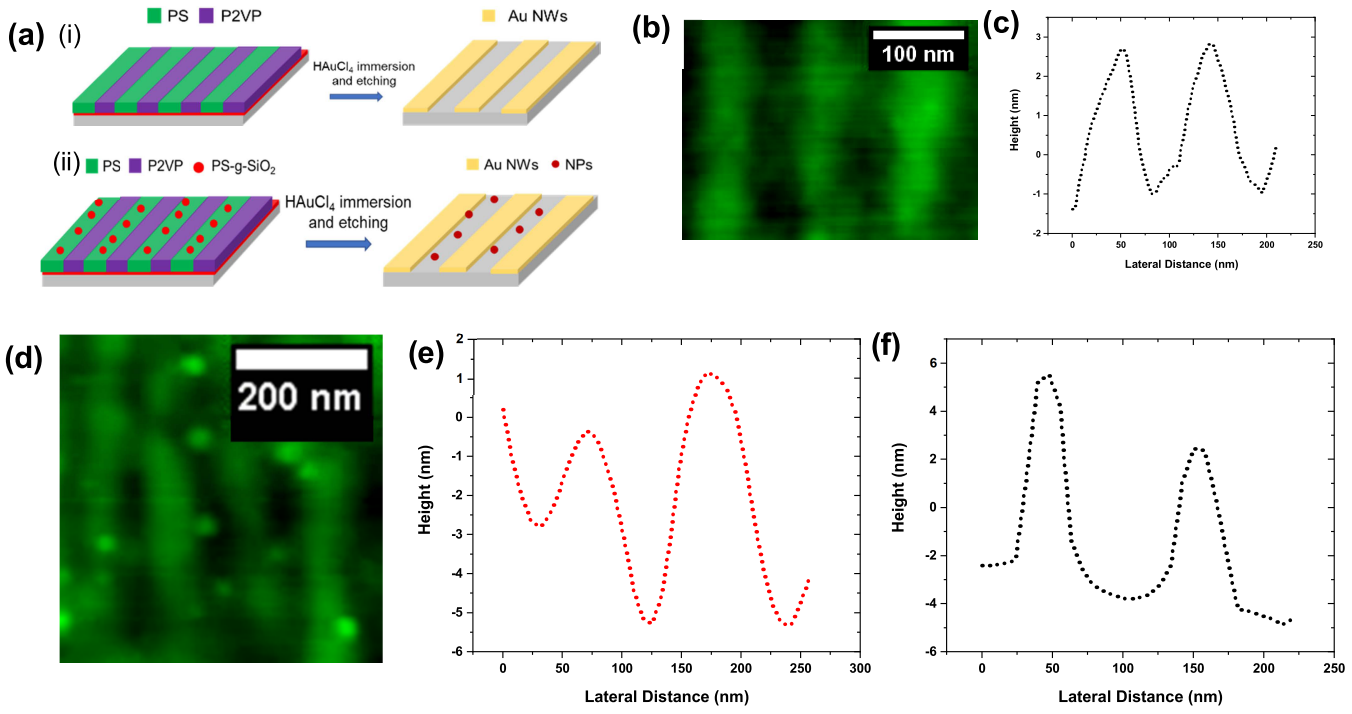

Figure 7. Metallic nanowire−dielectric nanoparticle hybrid nanostructures by the metallization and etching of the aligned high-molecular-mass BCP-PGNP blends. (a) Schematics of the metallization and etching of the aligned BCP-PGNP blends. (b) AFM image of aligned gold nanowires derived from high-molecular-weight *l*-BCP without the nanoparticles. (c) Height profile of the nanowires shown in (b) showing ≈100 nm domain size. (d) AFM image showing hybrid nanowire−nanoparticle structures derived from etching aligned high-molecular-mass BCP-PGNP blends. (e) Height profile of the nanowires shown in (d) showing ≈100 nm domain size. (f) Height profile of nanoparticles shown in (d) showing nanoparticles with ≈16 nm diameter.

monomers per chain, and a grafting density of 0.64 nm^{-2}. Interestingly, we observe complete alignment for *l*-BCP-PGNP blends at PGNP concentrations as high as 10 mass % w.r.t the BCP, as shown in Figure 6. Figure 6a shows the schematic for the alignment of *l*-BCP/PGNP blends. Figure 6b,c shows the aligned *l*-BCP/PGNP blend along the shear direction, with the PGNPs localized in the PS domain of the BCP. Figure 6c is the color-enhanced image of Figure 6b showing the PGNPs in the

https://doi.org/10.1021/acsami.1c23865
ACS Appl. Mater. Interfaces 2022, 14, 12824−12835

BCP domains. Furthermore, Figure 6b,c shows the asymmetric swelling of BCP domains due to the presence of PGNPs in the PS domain of the BCP. The complete localization and alignment of *l*-BCP-PGNP blends, in this case, might be facilitated by the relatively small change in the BCP viscosity and mobility upon PGNP addition since the BCPs used in this case have high molecular mass. It should be pointed out that the phase separation and alignment of neat high-molecular mass BCP is challenging by other techniques[53−55] due to their high viscosity. However, in our case, we observe phase separation as well as alignment of high-molecular mass BCP/PGNP blend despite their high viscosity. The phase separation and alignment of high-molecular mass BCP-PGNP blends might be facilitated by the low thickness (≈30 nm) of the BCP film used in this study. Furthermore, the complete segregation of the PGNP to the PS domain in contrast with the previous studies[51] might be a result of the high ratio of the half domain width of the swollen blends to the PGNP size, which in our case is ≈2. Additionally, the low interfacial width due to high χN and the lamellar nature of these films might have a beneficial effect on the PGNP localization and alignment. It should be highlighted here that NPs appear to be more predominant on the surface (visible in AFM height images). It is possible that NPs might move to the surface by evaporation front effects due to PS brush solubility with the solvent (toluene) or the NP might be squeezed to the surface to avoid entropic squeeze by the P2VP blocks.

Hybrid Nanowire−Nanoparticle Structures from Aligned *l*-BCP/PGNP Blends. The hybrid nanowire−nanoparticle structures are visioned to have unique photonic and electronics properties needed for futuristic applications. The localization of the PGNPs in one of the BCP domains gives a unique opportunity for making nanowire−nanoparticle hybrid nanostructures by converting one domain to metallic nanowire and etching off the organic content. Previously,[5,28,29] hybrid nanostructures have been demonstrated using multilayering of BCP and metal infiltration. However, the multilayered structures suffer from the possibility of random placement of the nanoparticles and are limited to only the nanoparticles, which can be made by atom or ion intercalation with the polymer. On the other hand, aligned *l*-BCP-PGNP blends can be used for hybrid structures, wherein nanowires can be generated by intercalation of ions or atoms and nanoparticles can be generated using PGNPs. Given the recent developments in polymer grafting, a plethora of nanoparticles can be used in hybrid nanostructures including liquid metal nanoparticles,[56] magnetic nanoparticles,[57] plasmonic nanoparticles,[58] etc., and low aspect ratio nanowires[58] as well.

Figure 7a(i,ii) shows the schematics for converting the BCP and *l*-BCP/PGNP blends to nanowires and hybrid metallic nanowire−dielectric nanoparticle nanostructures, respectively. The nanowires for high-molecular-mass BCP (PS-*b*-P2VP with M_w 133,000-*b*-132,000) are generated by the process described in Figure 5 using liquid phase infiltration of gold into P2VP channels and organic content etching. Similarly, hybrid structures were generated by liquid phase gold infiltration and organic content etching of *l*-BCP-PGNP-aligned blend films. Figure 7b,c shows the aligned gold nanowires for high-molecular mass block copolymer templates and their height profiles (Figure S7a), respectively, after gold infiltration and organic etching. The nanowires have an average width of ≈50 nm. Figure 7d shows the hybrid gold nanowire−silica nanoparticle nanostructures derived from aligned *l*-BCP/PGNP blends. While not highly ordered, nanoparticles, on average, are present on the edges of the nanowires along with the distribution in between the nanowires. The swelling of P2VP domains during the gold infiltration as described in Figure 5 might contribute to the folding of P2VP chains on PGNPs, thus resulting in the presence of the nanoparticles close to the nanowires. Figure 7e shows the height profile of the nanowires (90° to the long axis of the nanowires) shown in Figure 7d, showing ≈50 nm nanowires (Figure S7b). Figure 7f shows the height profile of SiO_2 nanoparticles (between the nanowires) in the hybrid nanostructures shown in Figure 7d, showing nanoparticles having ≈16 nm diameter (Figure S7c).

Gold nanowires are very promising for biosensing or chemical sensing applications,[59,60] wherein detection of molecules can be performed by electrochemical property change or optical property change during the biomolecule or chemical interaction with the nanowires. In between electrochemical and optical bio/chemical sensing, optical methods have the advantage of simpler device fabrication and easier measurement. However, it is difficult to tune the plasmonic response of the aligned gold nanowires for desired applications. On the other hand, the optical resonance of the nanoparticles has been tuned using dielectric cores and metallic shells in pioneering work by the Halas group.[61]

Here, we show that the optical absorption of gold nanowires can be tuned by the presence of dielectric nanoparticles in hybrid metallic gold nanowires/dielectric SiO_2 nanoparticles derived from aligned *l*-BCP/PGNP blends. Figure 8 shows the optical absorption spectra from the neat gold nanowires and hybrid nanowire−nanoparticle structures. The neat gold nanowires show an absorption peak around 535 nm, as shown in the black curve in Figure 8. The hybrid nanostructures show an absorption peak around 550 nm, as shown in the red curve in Figure 8, demonstrating a "red shift" in the plasmonic response of hybrid nanostructures. The observed "red shift" in hybrid nanostructures might be explained by analogy to dielectric core-metal nanoshell structures.[61,62] It is well established that the presence of a dielectric media screens the coulomb forces between the positive lattice and the oscillating electrons.[62] In

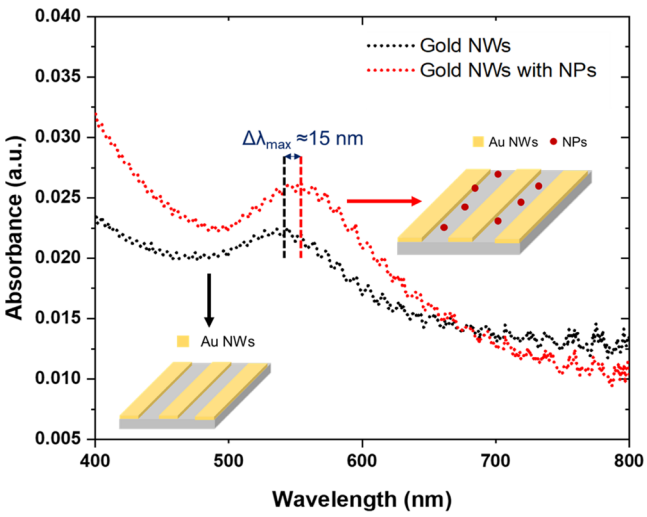

Figure 8. UV−vis absorption spectra of gold nanowires without (shown in black) and with (shown in red) the presence of dielectric SiO_2 nanoparticles. The presence of SiO_2 nanoparticles results in a marked shift in the absorption spectrum of gold nanowires, with a 15 nm shift for the peak absorption wavelength.

https://doi.org/10.1021/acsami.1c23865
ACS Appl. Mater. Interfaces 2022, 14, 12824−12835

this case, the addition of dielectric nanoparticles contributes to an increase in the effective dielectric constant[62] of the media, thus causing the "red shift" of the plasmonic energy. Furthermore, the presence of dielectric nanoparticles in hybrid nanostructures increases the plasmonic absorption intensity as well. This tuning of the plasmonic response of aligned gold nanowires by the presence of dielectric nanoparticles has the promise of designing robust bio/chemical sensing architectures for simultaneous control over biomolecule or chemical adhesion as well as their optical resonances. Furthermore, given that the PGNP localization and alignment are affected by polymer ligands and not the core, PGNP cores can be judiciously selected to incorporate additional magnetic, electronic, and optical property control.

CONCLUSIONS

In conclusion, we have demonstrated the ability of scalable and roll-to-roll processible template-free macroscopic alignment of lamellar BCPs for sub-10 nm patterning, paving the way for much easier integration of *l*-BCPs, especially as compared to *c*-BCPs, for the lithography industry's need for high-resolution line patterns and with high line-space utilization. This is enabled by the soft-shear-directed self-assembly of lamellar diblock PS-*b*-P2VP and triblock P2VP-*b*-PS-*b*-P2VP BCPs, with a straightforward dual-surface neutralization with high-molecular mass PMMA polymer, that also transmits the shear generated by cold zone annealing in soft shear mode. Subsequent incorporation of gold from its solution phase into the BCPs generates macroscopically aligned gold nanowires with spacings as small as 7 nm, which can serve as critical-dimension templates for next-generation lithography. Furthermore, we use the soft-shear strategy to shear align *l*-BCP/PGNP blends by incorporating PS-*g*-SiO_2 PGNPs in a high-molecular mass lamellar BCP matrix. We use these aligned *l*-BCP-PGNP blends to generate hybrid metallic gold nanowire−dielectric SiO_2 nanoparticle nanostructures by ion infiltration and dry etching. The hybrid nanostructures show a red shift in plasmonic response as compared to neat gold nanowires, which could be useful for designing next-generation bio/chemical sensing devices.

EXPERIMENTAL SECTION

Materials. Polystyrene-*block*-poly(2-vinyl pyridine) (PS-*b*-P2VP) (mol. mass 25-*b*-25 kg/mol, 133,000-*b*-132,000 kg/mol) and poly(2-vinyl pyridine)-*block*-polystyrene-*block*-poly(2-vinyl pyridine) (P2VP-*b*-PS-*b*-P2VP) (mol. mass 9.5-*b*-17.5-*b*-9.5 kg/mol) were purchased from Polymer Source Inc. and used as received. Poly(methyl methacrylate) (PMMA) (mol. mass 600 kg/mol) was purchased from Agilent and used without any further purification. Quartz substrates (3 in. × 1 in., thickness ≈0.7 mm) were purchased from GM associates. Toluene, poly(styrene sulfonate) (PSS) (molecular mass 75 kg/mol) solution (18 mass % in water), used for sacrificial film coating, and chloroauric acid (gold(III) chloride hydrate or $HAuCl_4$) were purchased from Sigma-Aldrich and used as received. Sylgard-184 elastomer (poly(dimethylsiloxane) along with the cross-linker) was purchased from Dow Corning. The PGNPs used in this study are synthesized using atom transfer radical polymerization (ATRP), and the synthesis details are mentioned elsewhere.[52] Briefly, PS-*g*-SiO_2 PGNPs have ≈16 nm SiO_2 cores, an average of 360 monomers per chain, and a grafting density of 0.64 nm^{-2}.

Methods. Quartz substrates were UV Ozone treated for 2 h before using to clean and increase the surface energy to 75 mJ/m^2. PMMA was mixed with toluene, and films with thicknesses ≈18 nm were flow/spin-coated over quartz substrates. The PMMA films were annealed in vacuum at 220 °C for 30 min to ensure the adsorption of PMMA chains to the substrate. The adsorption of the chains was confirmed by washing the films with toluene, wherein no decrease of film thickness was observed. The *l*-BCPs or *l*-BCP-PGNP (10 (mass/mass) % PS-*g*-SiO_2 w.r.t PS-*b*-P2VP) blends were dissolved in toluene and flow/spin coated (thickness ≈30−40 nm) over the PMMA films. Sacrificial PSS (thickness ≈24 nm) was flow/spin coated over silicon substrates. PMMA films of thickness ≈24 nm were flow/spin coated over the PSS films. The PMMA films were floated in water and picked on the BCP or blend films. The BCP or blend films were sandwiched between two neutral surfaces with this strategy. The PDMS elastomer was mixed with the cross-linker (mass ratio 10:1), stirred vigorously, and degassed under vacuum to take out the air bubbles. Then, the PDMS solution was poured over glass slides with a thickness of ≈0.5 mm and cured at 60 °C for 12 h. The cross-linked PDMS pads were peeled off and attached to the polymer films. Six millimolar solution of chloroauric acid ($HAuCl_4$) in water was prepared. PS-*b*-P2VP or blend films were immersed inside the aqueous $HAuCl_4$ for 24 h to saturate P2VP domains with gold. After taking out the PS-*b*-P2VP films from the gold bath, the films were gently sonicated in deionized water for 20−30 s to remove the residual gold layer at the surface prior to UVO etching. P2VP-*b*-PS-*b*-P2VP was immersed in the $HAuCl_4$ bath for 15 min. On immersion of P2VP-*b*-PS-*b*-P2VP for longer times, domains merged, probably due to smaller domain size and predominant out-of-plane swelling. Furthermore, the sonication of P2VP-*b*-PS-*b*-P2VP post dipping in the gold bath also resulted in the merging of nanochannels. So, the P2VP-*b*-PS-*b*-P2VP films were repeatedly rinsed in deionized water for 1 min to remove the residual gold layer before UVO etching. The UVO etching was performed using Novascan UVO system in the air for 30 min and etching rates of 2 nm/s were observed on control samples.

Cold Zone Annealing. The hot zone was created by electrically heated nickel chromium wire (resistivity—0.025 Ω cm) having a 3 mm diameter. The wire was insulated by ceramic insulation, having an outside diameter of 5 mm. The wire was heated by a Volteq DC power source. The hot wire was sandwiched between two movable aluminum blocks cooled by ethylene glycol and water mixture at a temperature of 10 °C. The coolant was circulated by a chiller. The aluminum blocks are 0.5 mm from the insulated hot wire. This setup generates a maximum temperature of 210 °C and a temperature gradient of 50 °C/mm over 0.7 mm thick quartz substrate. The temperature profile is shown in the Supporting Information, Figure S2. The BCP films were translated at a speed of 0.05 mm/s over the CZA setup. The distance of the BCP film in the melt state is 5 mm (Supporting Information, Figure S2). The annealing times are (time = distance in the melt state/speed) 100 s in this study.

Characterization. The film thicknesses were characterized using an F3-UV filmetrics interferometer. The topography of the BCP or blend films was characterized using a Dimension Icon atomic force microscope (AFM) in the tapping mode. The PMMA topcoat was etched using UVO etching before the AFM characterization. Typical etching rates observed were 2 nm/s using UVO etching. The images are digitized using NIH ImageJ. A negative high mass resolution depth profile was performed using a TOF-SIMS NCS instrument, which combines a TOF.SIMS.5 instrument (ION-TOF GmbH, Münster, Germany) and an in situ scanning probe microscope (NanoScan, Switzerland) at Shared Equipment Authority from Rice University. A bunched 30 keV Bi_3^+ ions (with a measured current of 0.15 pA) were used as a primary probe for analysis (scanned area 100 × 100 μm^2), and sputtering was performed using Ar_{1500}^+ ions at 10 keV with a typical current around 0.1 nA, rastered area 500 × 500 μm^2. The beams were operated in a noninterlaced mode, alternating one analysis cycle and one sputtering cycle (corresponding to 1.63 s) followed by a pause of 3 s for the charge compensation with an electron flood gun. An adjustment of charge effects has been operated using a surface potential of 0 V and an extraction bias of −20 V. During the depth profiling, the cycle time was fixed to 200 μs (corresponding to m/z = 0−3644 a.m.u. mass range). The grazing incidence small-angle X-ray scattering (GISAXS) measurements were performed on BCP films confined between the top and bottom PMMA layer after CZA-SS. The GISAXS data are shown at an incidence angle of 0.12° for both PS-*b*-P2VP and P2VP-*b*-PS-*b*-P2VP at a random location on 1 in. × 1 in. wafer. The GISAXS

https://doi.org/10.1021/acsami.1c23865
ACS Appl. Mater. Interfaces 2022, 14, 12824−12835

measurements for PS-*b*-P2VP BCP were performed at beamline 8-ID-E[63] of Advanced Photon Source of Argonne National Lab. The X-ray energy was 10.9 keV, the Dectris Pilatus 1 M pixel array detector was placed at 2185 mm from the sample, and the data was analyzed using GIXSGUI[64] software in MATLAB, developed at beamline 8-ID-E. The GISAXS measurements for P2VP-*b*-PS-*b*-P2VP were performed at beamline 7.3.3[65] of Advanced Light Source at Lawrence Berkeley National Lab at an X-ray energy of 10 keV using a Pilatus 1 M detector. The data were analyzed using the Igor Pro NIKA package.[66] The energy-dispersive X-ray analysis was performed using a JOEL JSM-7600 F scanning electron microscope. The UV−visible spectroscopy was performed using Evolution 201 UV−visible spectrophotometer.

■ ASSOCIATED CONTENT

Supporting Information

The Supporting Information is available free of charge at https://pubs.acs.org/doi/10.1021/acsami.1c23865.

Demonstration of the ability of vertically oriented and unidirectionally aligned lamellar BCPs (Figure S1); temperature profile over the quartz substrate (Figure S2); effect of topcoat molecular mass on the block copolymer (BCP) alignment (Figure S3); AFM height image of gold nanowires (Figure S4); the AFM images showing aligned gold nanowires (Figure S5); energy-dispersive X-ray analysis of gold nanochannels (Figure S6); the AFM images showing aligned gold nanowires and hybrid nanostructures (Figure S7); and solvent (toluene) wash test (Figure S8) (PDF)

■ AUTHOR INFORMATION

Corresponding Author

Alamgir Karim − *Department of Chemical and Biomolecular Engineering, University of Houston, Houston, Texas 77204, United States;* orcid.org/0000-0003-1302-9374; Email: akarim3@central.uh.edu

Authors

Maninderjeet Singh − *Department of Chemical and Biomolecular Engineering, University of Houston, Houston, Texas 77204, United States;* orcid.org/0000-0001-8891-8454

Aman Agrawal − *Department of Chemical and Biomolecular Engineering, University of Houston, Houston, Texas 77204, United States*

Wenjie Wu − *Department of Chemical and Biomolecular Engineering, University of Houston, Houston, Texas 77204, United States*

Ali Masud − *Department of Chemical and Biomolecular Engineering, University of Houston, Houston, Texas 77204, United States;* orcid.org/0000-0001-7619-4364

Edward Armijo − *Department of Chemical and Biomolecular Engineering, University of Houston, Houston, Texas 77204, United States;* orcid.org/0000-0001-5242-0806

Damian Gonzalez − *Department of Chemical and Biomolecular Engineering, University of Houston, Houston, Texas 77204, United States*

Shenghui Zhou − *Materials Science Program, University of Houston, Houston, Texas 77204, United States*

Tanguy Terlier − *SIMS Laboratory, Shared Equipment Authority, Rice University, Houston, Texas 77005, United States;* orcid.org/0000-0002-4092-0771

Chenhui Zhu − *Advanced Light Source, Lawrence Berkeley National Lab, Berkeley, California 94720, United States*

Joseph Strzalka − *X-Ray Science Division, Argonne National Laboratory, Lemont, Illinois 60439, United States;* orcid.org/0000-0003-4619-8932

Krzysztof Matyjaszewski − *Department of Chemistry, Carnegie Mellon University, Pittsburgh, Pennsylvania 15213, United States;* orcid.org/0000-0003-1960-3402

Michael Bockstaller − *Department of Materials Science and Engineering, Carnegie Mellon University, Pittsburgh, Pennsylvania 15213, United States;* orcid.org/0000-0001-9046-9539

Jack F. Douglas − *Material Science and Engineering Division, National Institute of Standards and Technology (NIST), Gaithersburg, Maryland 20899, United States;* orcid.org/0000-0001-7290-2300

Complete contact information is available at: https://pubs.acs.org/10.1021/acsami.1c23865

Notes

Certain commercial materials and equipment are identified to specify adequately the experimental procedure. In no case does such identification imply a recommendation by the National Institute of Standards and Technology nor does it imply that the material or equipment identified is necessarily the best available for this purpose.

The authors declare no competing financial interest.

Additional data supporting this paper are available from the corresponding author upon reasonable request.

■ ACKNOWLEDGMENTS

A.K. acknowledges NSF DMR-1905996 for funding this research. A.K., M.B., and K.M. acknowledge DOE-BES−DE-SC0018854 for the PGNP aspects of the work. ToF-SIMS analyses were carried out with support provided by the National Science Foundation CBET-1626418. This work was conducted in part using resources of the Shared Equipment Authority at Rice University. The authors acknowledge the use of resources of the Advanced Photon Source, a U.S. Department of Energy (DOE) Office of Science User Facility operated for the DOE Office of Science by Argonne National Laboratory under Contract No. DE-AC02-06CH11357. The authors also acknowledge the use of beamline 7.3.3 of the Advanced Light Source, which is a DOE Office of Science User Facility under contract no. DE-AC02-05CH11231.

■ REFERENCES

(1) Suh, H. S.; Kim, D. H.; Moni, P.; Xiong, S.; Ocola, L. E.; Zaluzec, N. J.; Gleason, K. K.; Nealey, P. F. Sub-10-Nm Patterning via Directed Self-Assembly of Block Copolymer Films with a Vapour-Phase Deposited Topcoat. *Nat. Nanotechnol.* **2017**, *12*, 575−581.

(2) Liu, C.-C.; Franke, E.; Mignot, Y.; Xie, R.; Yeung, C. W.; Zhang, J.; Chi, C.; Zhang, C.; Farrell, R.; Lai, K.; Tsai, H.; Felix, N.; Corliss, D. Directed Self-Assembly of Block Copolymers for 7 Nanometre FinFET Technology and Beyond. *Nat. Electron.* **2018**, *1*, 562−569.

(3) Kim, J. H.; Jin, H. M.; Yang, G. G.; Han, K. H.; Yun, T.; Shin, J. Y.; Jeong, S. J.; Kim, S. O. Smart Nanostructured Materials Based on Self-Assembly of Block Copolymers. *Adv. Funct. Mater.* **2020**, *30*, No. 1902049.

(4) Thurn-Albrecht, T.; Schotter, J.; Kastle, G. A.; Emley, N.; Shibauchi, T.; Krusin-Elbaum, L.; Guarini, K.; Black, C. T.; Tuominen, M. T.; Russell, T. P. Ultrahigh-Density Nanowire Arrays Grown in Self-Assembled Diblock Copolymer Templates. *Science* **2000**, *290*, 2126−2129.

(5) Shin, D. O.; Yun, J. M.; Yang, Y.; Oh, Y.; Lee, J. Y.; Shin, J.; Lee, K. J.; Park, S.; Kim, J. U.; Kim, S. O.; et al. Multicomponent Nanopatterns

by Directed Block Copolymer Self-Assembly. *ACS Nano* **2013**, *7*, 8899−8907.
(6) Ouk Kim, S.; Solak, H. H.; Stoykovich, M. P.; Ferrier, N. J.; De Pablo, J. J.; Nealey, P. F. Epitaxial Self-Assembly of Block Copolymers on Lithographically Defined Nanopatterned Substrates. *Nature* **2003**, *424*, 411−414.
(7) Stoykovich, M. P.; Müller, M.; Kim, S. O.; Solak, H. H.; Erik, W.; De Pablo, J. J.; Nealey, P. F. Directed Assembly of Block Copolymer Blends into Nonregular Device-Oriented Structures. *Science* **2005**, *308*, 1442−1446.
(8) Ruiz, R.; Kang, H.; Detcheverry, F. A.; Dobisz, E.; Kercher, D. S.; Albrecht, T. R.; De Pablo, J. J.; Nealey, P. F. Density Multiplication and Improved Lithography by Directed Block Copolymer Assembly. *Science* **2008**, *321*, 936−939.
(9) Tavakkoli KG, A.; Gotrik, K. W.; Hannon, A. F.; Alexander-Katz, A.; Ross, C. A.; Berggren, K. K. Templating Three-Dimensional Self-Assembled Structures in Bilayer Block Copolymer Films. *Science* **2012**, *336*, 1294−1298.
(10) Bita, I.; Joel, K.; Yang, W.; Yeon Sik Jung, C. A. R.; Edwin, L.; Thomas, K. K. B. Graphoepitaxy of Self-Assembled Block Copolymers on Two-Dimensional Periodic Patterned Templates. *Science* **2008**, *321*, 939−944.
(11) Segalman, R. A.; Yokoyama, H.; Kramer, E. J. Graphoepitaxy of Spherical Domain Block Copolymer Films. *Adv. Mater.* **2001**, *13*, 1152−1155.
(12) Singh, M.; Wu, W.; Basutkar, M. N.; Strzalka, J.; Al-Enizi, A. M.; Douglas, J. F.; Karim, A. Ultra-Fast Vertical Ordering of Lamellar Block Copolymer Films on Unmodified Substrates. *Macromolecules* **2021**, *54*, 1564−1573.
(13) Singh, M.; Wu, W.; Nuka, V.; Strzalka, J.; Douglas, J. F.; Karim, A. Late Stage Domain Coarsening Dynamics of Lamellar Block Copolymers. *ACS Macro Lett.* **2021**, *10*, 727−731.
(14) Hayirlioglu, A.; Kulkarni, M.; Singh, G.; Al-Enizi, A. M.; Zvonkina, I.; Karim, A. Block Copolymer Ordering on Elastomeric Substrates of Tunable Surface Energy. *Emergent Mater.* **2019**, *2*, 11−22.
(15) Singh, G.; Yager, K. G.; Berry, B.; Kim, H. C.; Karim, A. Dynamic Thermal Field-Induced Gradient Soft-Shear for Highly Oriented Block Copolymer Thin Films. *ACS Nano* **2012**, *6*, 10335−10342.
(16) Alvarez-Fernandez, A.; Cummins, C.; Saba, M.; Steiner, U.; Fleury, G.; Ponsinet, V.; Guldin, S. Block Copolymer Directed Metamaterials and Metasurfaces for Novel Optical Devices. *Adv. Opt. Mater.* **2021**, *9*, No. 2100175.
(17) Wang, Z.; Chan, C. L. C.; Zhao, T. H.; Parker, R. M.; Vignolini, S. Recent Advances in Block Copolymer Self-Assembly for the Fabrication of Photonic Films and Pigments. *Adv. Opt. Mater.* **2021**, *9*, No. 2100519.
(18) Liu, C.-C.; Franke, E.; Mignot, Y.; LeFevre, S.; Sieg, S.; Chi, C.; Meli, L.; Parnell, D.; Schmidt, K.; Sanchez, M.; Singh, L.; Furukawa, T.; Seshadri, I.; De Silva, E. A.; Tsai, H.; Lai, K.; Truong, H.; Farrell, R.; Bruce, R.; Somervell, M.; Sanders, D.; Felix, N.; Arnold, J.; Hetzer, D.; Ko, A.; Metz, A.; Colburn, M.; Corliss, D. In *DSA Patterning Options for Logics and Memory Applications*, Advances in Patterning Materials and Processes XXXIV; International Society for Optics and Photonics, 2017; Vol. *10146*, p 1014603.
(19) Yoo, H. G.; Byun, M.; Jeong, C. K.; Lee, K. J. Performance Enhancement of Electronic and Energy Devices via Block Copolymer Self-Assembly. *Adv. Mater.* **2015**, *27*, 3982−3998.
(20) Ouk Kim, S.; Solak, H. H.; Stoykovich, M. P.; Ferrier, N. J.; De Pablo, J. J.; Nealey, P. F. Epitaxial Self-Assembly of Block Copolymers on Lithographically Defined Nanopatterned Substrates. *Nature* **2003**, *424*, 411−414.
(21) Wan, L.; Ruiz, R.; Gao, H.; Patel, K. C.; Albrecht, T. R.; Yin, J.; Kim, J.; Cao, Y.; Lin, G. The Limits of Lamellae-Forming PS- b -PMMA Block Copolymers for Lithography. *ACS Nano* **2015**, *9*, 7506−7514.
(22) Bates, C. M.; Seshimo, T.; Maher, M. J.; Durand, W. J.; Cushen, J. D.; Dean, L. M.; Blachut, G.; Ellison, C. J.; Willson, C. G. Polarity-Switching Top Coats Enable Copolymer Domains. *Science* **2012**, *338*, 775−779.
(23) Lane, A. P.; Yang, X.; Maher, M. J.; Blachut, G.; Asano, Y.; Someya, Y.; Mallavarapu, A.; Sirard, S. M.; Ellison, C. J.; Willson, C. G. Directed Self-Assembly and Pattern Transfer of Five Nanometer Block Copolymer Lamellae. *ACS Nano* **2017**, *11*, 7656−7665.
(24) Sacanna, S.; Irvine, W. T. M.; Chaikin, P. M.; Pine, D. J. Lock and Key Colloids. *Nature* **2010**, *464*, 575−578.
(25) Wang, Y.; Wang, Y.; Breed, D. R.; Manoharan, V. N.; Feng, L.; Hollingsworth, A. D.; Weck, M.; Pine, D. J. Colloids with Valence and Specific Directional Bonding. *Nature* **2012**, *491*, 51−55.
(26) Leunissen, M. E.; Christova, C. G.; Hynninen, A. P.; Royall, C. P.; Campbell, A. I.; Imhof, A.; Dijkstra, M.; Van Roij, R.; Van Blaaderen, A. Ionic Colloidal Crystals of Oppositely Charged Particles. *Nature* **2005**, *437*, 235−240.
(27) Xia, Y.; Nguyen, T. D.; Yang, M.; Lee, B.; Santos, A.; Podsiadlo, P.; Tang, Z.; Glotzer, S. C.; Kotov, N. A. Self-Assembly of Self-Limiting Monodisperse Supraparticles from Polydisperse Nanoparticles. *Nat. Nanotechnol.* **2011**, *6*, 580−587.
(28) Rahman, A.; Majewski, P. W.; Doerk, G.; Black, C. T.; Yager, K. G. Non-Native Three-Dimensional Block Copolymer Morphologies. *Nat. Commun.* **2016**, *7*, No. 13988.
(29) Park, T. W.; Jung, H.; Park, J.; Ahn, Y.; Hong, S. W.; Lee, J.; Lee, J.; Park, W. I. Topographically Designed Hybrid Nanostructures via Nanotransfer Printing and Block Copolymer Self-Assembly. *Nanoscale* **2021**, *13*, 11161−11168.
(30) Angelescu, D. E.; Waller, J. H.; Adamson, D. H.; Deshpande, P.; Chou, S. Y.; Register, R. A.; Chaikin, P. M. Macroscopic Orientation of Block Copolymer Cylinders in Single-Layer Films by Shearing. *Adv. Mater.* **2004**, *16*, 1736−1740.
(31) Singh, G.; Yager, K. G.; Berry, B.; Kim, H. C.; Karim, A. Dynamic Thermal Field-Induced Gradient Soft-Shear for Highly Oriented Block Copolymer Thin Films. *ACS Nano* **2012**, *6*, 10335−10342.
(32) Majewski, P. W.; Rahman, A.; Black, C. T.; Yager, K. G. Arbitrary Lattice Symmetries via Block Copolymer Nanomeshes. *Nat. Commun.* **2015**, *6*, No. 7448.
(33) Pujari, S.; Keaton, M. A.; Chaikin, P. M.; Register, R. A. Alignment of Perpendicular Lamellae in Block Copolymer Thin Films by Shearing. *Soft Matter* **2012**, *8*, 5358−5363.
(34) Kim, D. H.; Kim, S. Y. Universal Interfacial Control through Polymeric Nanomosaic Coating for Block Copolymer Nanopatterning. *ACS Nano* **2020**, *14*, 7140−7151.
(35) Oh, J.; Shin, M.; Kim, I. S.; Suh, H. S.; Kim, Y.; Kim, J. K.; Bang, J.; Yeom, B.; Son, J. G. Shear-Rolling Process for Unidirectionally and Perpendicularly Oriented Sub-10-Nm Block Copolymer Patterns on the 4 in Scale. *ACS Nano* **2021**, *15*, 8549−8558.
(36) Hore, M. J. A.; Korley, L. S. T. J.; Kumar, S. K. Polymer-Grafted Nanoparticles. *J. Appl. Phys.* **2020**, *128*, No. 030401.
(37) Wu, W.; Singh, M.; Masud, A.; Wang, X.; Nallapaneni, A.; Xiao, Z.; Zhai, Y.; Wang, Z.; Terlier, T.; Bleuel, M.; Yuan, G.; Satija, S. K.; Douglas, J. F.; Matyjaszewski, K.; Bockstaller, M. R.; Karim, A. Control of Phase Morphology of Binary Polymer Grafted Nanoparticle Blend Films via Direct Immersion Annealing. *ACS Nano* **2021**, *15*, 12042−12056.
(38) Yoshida, H.; Suh, H. S.; Ramírez-Hernández, A.; Lee, J. I.; Aida, K.; Wan, L.; Ishida, Y.; Tada, Y.; Ruiz, R.; de Pablo, J.; Nealey, P. F. Topcoat Approaches for Directed Self-Assembly of Strongly Segregating Block Copolymer Thin Films. *J. Photopolym. Sci. Technol.* **2013**, *26*, 55−58.
(39) Chai, J.; Wang, D.; Fan, X.; Buriak, J. M. Assembly of Aligned Linear Metallic Patterns on Silicon. *Nat. Nanotechnol.* **2007**, *2*, 500−506.
(40) Li, L.; Liu, X.; Pal, S.; Wang, S.; Ober, C. K.; Giannelis, E. P. Extreme Ultraviolet Resist Materials for Sub-7 Nm Patterning. *Chem. Soc. Rev.* **2017**, *46*, 4855−4866.
(41) Ha, D.; Yang, C.; Lee, J.; Lee, S.; Lee, S. H.; Seo, K. I.; Oh, H. S.; Hwang, E. C.; Do, S. W.; Park, S. C.; Sun, M. C.; Kim, D. H.; Lee, J. H.; Kang, M. I.; Ha, S. S.; Choi, D. Y.; Jun, H.; Shin, H. J.; Kim, Y. J.; Lee, J.; Moon, C. W.; Cho, Y. W.; Park, S. H.; Son, Y.; Park, J. Y.; Lee, B. C.; Kim, C.; Oh, Y. M.; Park, J. S.; Kim, S. S.; Kim, M. C.; Hwang, K. H.; Nam, S. W.; Maeda, S.; Kim, D. W.; Lee, J. H.; Liang, M. S.; Jung, E. S.

https://doi.org/10.1021/acsami.1c23865
ACS Appl. Mater. Interfaces 2022, 14, 12824−12835

In *Highly Manufacturable 7nm FinFET Technology Featuring EUV Lithography for Low Power and High Performance Applications*, Digest of Technical Papers - Symposium on VLSI Technology; IEEE, 2017; pp T68−T69.
(42) Cummins, C.; Morris, M. A. Using Block Copolymers as Infiltration Sites for Development of Future Nanoelectronic Devices: Achievements, Barriers, and Opportunities. *Microelectron. Eng.* **2018**, *195*, 74−85.
(43) Hasan, R. M. M.; Luo, X. Promising Lithography Techniques for Next-Generation Logic Devices. *Nanomanuf. Metrol.* **2018**, *1*, 67−81.
(44) Leniart, A. A.; Pula, P.; Sitkiewicz, A.; Majewski, P. W. Macroscopic Alignment of Block Copolymers on Silicon Substrates by Laser Annealing. *ACS Nano* **2020**, *14*, 4805−4815.
(45) Mansky, P.; Liu, Y.; Huang, E.; Russell, T. P.; Hawker, C. Controlling Polymer-Surface Interactions with Random Copolymer Brushes. *Science* **1997**, *275*, 1458−1461.
(46) Masud, A.; Longanecker, M.; Bhadauriya, S.; Singh, M.; Wu, W.; Sharma, K.; Terlier, T.; Al-Enizi, A. M.; Satija, S.; Douglas, J. F.; Karim, A. Ionic Liquid Enhanced Parallel Lamellar Ordering in Block Copolymer Films. *Macromolecules* **2021**, *54*, 4531−4545.
(47) Masud, A.; Longanecker, M.; Bhadauriya, S.; Singh, M.; Wu, W.; Sharma, K.; Terlier, T.; Al-enizi, A. M.; Satija, S.; Douglas, J. F.; Karim, A. Ionic Liquid Enhanced Parallel Lamellar Ordering in Block Copolymer Films. *Macromolecules* **2021**, *54*, 4531−4545.
(48) Chen, X.; Delgadillo, P. R.; Jiang, Z.; Craig, G. S. W.; Gronheid, R.; Nealey, P. F. Defect Annihilation in the Directed Self-Assembly of Block Copolymers in Films with Increasing Thickness. *Macromolecules* **2019**, *52*, 7798−7805.
(49) Lee, J.; Mishra, A. K.; Choi, C.; Kim, D.; Kim, E. Y.; Yong, K.; Kim, J. K. Three-Dimensional Nanoporous Metal Structures from Poly(2-Vinylpyridine)- Block-Poly(4-Vinylpyridine) Copolymer Thin Film. *ACS Appl. Mater. Interfaces* **2020**, *12*, 15667−15674.
(50) Nie, Z.; Petukhova, A.; Kumacheva, E. Properties and Emerging Applications of Self-Assembled Structures Made from Inorganic Nanoparticles. *Nat. Nanotechnol.* **2010**, *5*, 15−25.
(51) Zhang, R.; Singh, G.; Dang, A.; Dai, L.; Bockstaller, M. R.; Akgun, B.; Satija, S.; Karim, A. Nanoparticle-Driven Orientation Transition and Soft-Shear Alignment in Diblock Copolymer Films via Dynamic Thermal Gradient Field. *Macromol. Rapid Commun.* **2013**, *34*, 1642−1647.
(52) Schmitt, M.; Zhang, J.; Lee, J.; Lee, B.; Ning, X.; Zhang, R.; Karim, A.; Davis, R. F.; Matyjaszewski, K.; Bockstaller, M. R. Polymer Ligand − Induced Autonomous Sorting and Reversible Phase Separation in Binary Particle Blends. *Sci. Adv.* **2016**, *2*, No. e1601484.
(53) Kim, E.; Ahn, H.; Park, S.; Lee, H.; Lee, M.; Lee, S.; Kim, T.; Kwak, E. A.; Lee, J. H.; Lei, X.; Huh, J.; Bang, J.; Lee, B.; Ryu, D. Y. Directed Assembly of High Molecular Weight Block Copolymers: Highly Ordered Line Patterns of Perpendicularly Oriented Lamellae with Large Periods. *ACS Nano* **2013**, *7*, 1952−1960.
(54) Samant, S.; Basutkar, M.; Singh, M.; Masud, A.; Grabowski, C. A.; Kisslinger, K.; Strzalka, J.; Yuan, G.; Satija, S.; Apata, I.; Raghavan, D.; Durstock, M.; Karim, A. Effect of Molecular Weight and Layer Thickness on the Dielectric Breakdown Strength of Neat and Homopolymer Swollen Lamellar Block Copolymer Films. *ACS Appl. Polym. Mater.* **2020**, *2*, 3072−3083.
(55) Singh, M.; Apata, I.; Samant, S.; Wu, W.; Tawade, B.; Pradhan, N.; Raghavan, D.; Karim, A. Nanoscale Strategies to Enhance the Energy Storage Capacity of Polymeric Dielectric Capacitors: Review of Recent Advances. *Polym. Rev.* **2021**, 1−50.
(56) Yan, J.; Malakooti, M. H.; Lu, Z.; Wang, Z.; Kazem, N.; Pan, C.; Bockstaller, M. R.; Majidi, C.; Matyjaszewski, K. Solution Processable Liquid Metal Nanodroplets by Surface-Initiated Atom Transfer Radical Polymerization. *Nat. Nanotechnol.* **2019**, *14*, 684−690.
(57) Jiao, Y.; Akcora, P. Assembly of Polymer-Grafted Magnetic Nanoparticles in Polymer Melts. *Macromolecules* **2012**, *45*, 3463−3470.
(58) Duan, H.; Yang, Y.; Zhang, Y.; Yi, C.; Nie, Z.; He, J. What Is next in Polymer-Grafted Plasmonic Nanoparticles? *Giant* **2020**, *4*, No. 100033.
(59) Spain, E.; McCooey, A.; Joyce, K.; Keyes, T. E.; Forster, R. J. Gold Nanowires and Nanotubes for High Sensitivity Detection of Pathogen DNA. *Sens. Actuators, B* **2015**, *215*, 159−165.
(60) Dawson, K.; Baudequin, M.; O'Riordan, A. Single On-Chip Gold Nanowires for Electrochemical Biosensing of Glucose. *Analyst* **2011**, *136*, 4507−4513.
(61) Oldenburg, S. J.; Averitt, R. D.; Westcott, S. L.; Halas, N. J. Nanoengineering of Optical Resonances. *Chem. Phys. Lett.* **1998**, *288*, 243−247.
(62) Jain, P. K.; El-Sayed, M. A. Surface Plasmon Resonance Sensitivity of Metal Nanostructures: Physical Basis and Universal Scaling in Metal Nanoshells. *J. Phys. Chem. C* **2007**, *111*, 17451−17454.
(63) Jiang, Z.; Li, X.; Strzalka, J.; Sprung, T. S.; Sun, T.; Sandy, A. R.; Narayanan, S.; Lee, D. R.; Wang, J. The dedicated high-resolution grazing-incidence X-ray scattering beamline 8-ID-E at the Advanced Photon Source. *J. Synchrotron Rad.* **2012**, *19*, 627−636.
(64) Jiang, Z. GIXSGUI: A MATLAB Toolbox for Grazing-Incidence X-Ray Scattering Data Visualization and Reduction, and Indexing of Buried Three-Dimensional Periodic Nanostructured Films. *J. Appl. Crystallogr.* **2015**, *48*, 917−926.
(65) Hexemer, A.; Bras, W.; Glossinger, J.; Schaible, E.; Gann, E.; Kirian, R.; MacDowell, A.; Church, M.; Rude, B.; Padmore, H. A SAXS/WAXS/GISAXS Beamline with Multilayer Monochromator. *J. Phys.: Conf. Ser.* **2010**, *247*, No. 012007.
(66) Ilavsky, J. Nika: software for two-dimensional data reduction. *J Appl Crystallogr* **2012**, *45* (2), 324−328.

https://doi.org/10.1021/acsami.1c23865
ACS Appl. Mater. Interfaces 2022, 14, 12824−12835